Progress In Electromagnetics Research B, Vol. 110, 43-56, 2025

(Received 26 October 2024, Accepted 30 December 2024, Scheduled 17 January 2025)

Compact Monopole Antenna with Cross Shaped Slot for Microwave Brain Tumor Detection Applications

Athul O. Asok[1], Mohanan Sowmya[2], Valiyaveetil U. Faisa[2], Fahima K. Fathima[2], A. I. Harikrishnan[2],
Mohan Sumi[2], and Sukomal Dey[1],*

[1]*Department of Electrical Engineering, Indian Institute of Technology Palakkad, Kerala-678623, India*
[2]*Department of Electronics and Communication Engineering, NSS College of Engineering Palakkad, Kerala-678008, India*

ABSTRACT: The early detection of brain tumors presents significant challenges due to the complexity of the brain as well as the need for noninvasive diagnostic tools. This study introduces a novel antenna design optimized for noninvasive brain tumor detection. In this work, a cross slotted circular patch with a rectangular slot in the ground plane is designed in the simulator for brain tumor detection. The designed antenna operates from 1.76 GHz to 13.6 GHz with an impedance matching of greater than -10 dB. The antenna attains a peak gain of 5.8 dBi at 8 GHz. The antenna has been fabricated using the Monolithic Microwave Integrated Circuit (MMIC) technology and then tested in an anechoic chamber environment. The simulated and measured antenna performance parameters are found in agreement. The developed antenna has been used to image a target containing liquid inside a bottle covered by foam material. The liquid inside the bottle mimics the tumor material as its dielectric constant is comparable to a realistic tumor material. The target has been successfully reconstructed using the Delay and Sum (DAS) approach.

1. INTRODUCTION

In 2024, brain tumors continue to pose a significant health challenge, with approximately 25,400 new cases of brain and other Central Nervous System (CNS) cancers expected in the United States, and about 18,760 deaths predicted from these malignancies. Although relatively rare, accounting for 1.3% of all new cancer cases, brain tumors are particularly concerning in paediatric and adolescent populations. They represent the third most common cancer and the third leading cause of cancer-related death in Adolescents and Young Adults (AYAs), with an estimated 12,800 new diagnoses annually in this group. Survival outcomes are heavily influenced by the tumor stage and type, with a five-year relative survival rate of 33.4% for brain and CNS tumors overall, increasing to 35.5% for localized tumors. Gliomas and meningiomas are among the most common tumor types, with glioblastomas being the most aggressive in adults over 40 years of age. Challenges in treatment persist due to the variability of tumor types and their behaviours across different age groups and demographics. Advancements in detection and treatment offer hope for improving outcomes, particularly for young adults, where over 90% survive five years post-diagnosis [1, 4].

Various brain imaging modalities are currently employed for the detection and characterization of brain tumors, each offering distinct advantages and limitations. Magnetic Resonance Imaging (MRI) is the most commonly used technique due to its superior soft tissue contrast, making it highly effective in identifying tumor boundaries and detecting smaller lesions. MRI, particularly with contrast agents, can provide detailed anatomical and functional information, although it is time-consuming and expensive. Computed Tomography (CT), while being faster and more widely available, lacks the soft tissue resolution of MRI but is often used in emergency settings for quick evaluations, especially when detecting calcifications or acute bleeding in tumors. Positron Emission Tomography (PET), often combined with CT or MRI, allows for metabolic imaging of tumors, providing insight into tumor aggressiveness and response to therapy. However, PET requires the use of radioactive tracers, which limits its repeated use and accessibility. Functional MRI (FMRI) and Diffusion Tensor Imaging (DTI) are advanced MRI techniques that assess brain function and white matter tracts, respectively, providing critical information for presurgical planning. Despite their value, these methods require high expertise and are not always available in routine clinical practice. Ultrasound, primarily used intraoperatively, offers real-time imaging during surgery but is limited by its low resolution in deep brain structures. Finally, Magnetoencephalography (MEG) and Electroencephalography (EEG) are used to assess brain activity, but their role in direct tumor detection is limited, serving mainly to localize functional areas of the brain. Each modality contributes uniquely, with the choice of imaging often dictated by clinical needs, availability, and the specific characteristics of the tumor [1–5].

Microwave imaging (MI), particularly using Ultra-Wideband (UWB) antennas, offers several advantages over traditional imaging modalities such as MRI, CT, and PET for brain tumor detection. Unlike these conventional techniques, MI is non-ionizing, making it safer for repeated use, especially in paediatric or long-term monitoring scenarios. It operates by exploiting the dielectric contrast between healthy

---

* Corresponding author: Sukomal Dey (sdey28@iitpkd.ac.in).

doi:10.2528/PIERB24102603 Published by THE ELECTROMAGNETIC ACADEMY

and malignant tissues, providing functional imaging of the tumor without the need for contrast agents or radioactive tracers. Furthermore, MI systems are significantly more cost-effective and compact, allowing for easier deployment in clinical settings or point-of-care facilities. The portability of MI devices also enables bedside or even home-based monitoring, a major advantage over MRI and CT, which require large, fixed installations.

UWB antennas are crucial for MI, offering high-resolution detection capabilities due to their broad frequency range, typically spanning from 3.1 to 10.6 GHz. UWB antennas provide improved penetration through biological tissues and can differentiate between various tissue types based on their electromagnetic properties. For brain tumor imaging, UWB systems can generate detailed, 3D reconstructions of the brain by capturing reflected signals from multiple angles, allowing for precise localization of the tumor. Additionally, UWB-based imaging systems can operate in real-time, making them suitable for intraoperative guidance or continuous monitoring of tumor progression. This dynamic capability distinguishes UWB antennas from static imaging modalities like MRI or CT, enabling real-time feedback during surgical procedures or treatment interventions [6].

MI systems typically employ one or more antennas to capture signals that are reflected or scattered from the target. These signals undergo processing to estimate the dielectric properties of the target, a method referred to as Microwave Tomography (MT) [7–10]. In MT, the signals are handled in the frequency domain, with antennas evenly distributed around the imaging region [11–13]. Advanced algorithms are used to estimate the dielectric properties of the target based on the reflected signals.

Another approach to MI is radar-based imaging, which identifies objects by processing reflected signals in the time domain. This technique offers faster processing and reduces computational demands. Examples of radar-based systems applied in biomedical imaging can be found in [14–16]. MI also has non-invasive applications in temperature monitoring during hyperthermia treatments, where the temperature of the tumor is elevated to approximately 44°C for a prolonged period [7]. In this context, MI tracks changes in dielectric properties that correspond to temperature fluctuations. Recent research has explored combining MT and radar-based techniques to harness the benefits of each. While MT offers a detailed dielectric profile to detect tumors or cancerous cells [17, 18], the radar-based method can be applied selectively to areas of concern, enhancing the speed of image reconstruction [17, 18].

These innovations bring new demands for antenna design. Antennas used in MI should ideally offer wide operational bandwidth, enhanced signal penetration, a high time-domain correlation factor, as well as increased gain and directivity. Various UWB antennas, including Vivaldi planar antennas [18, 19], double-ridged horn antennas [20, 21], planar monopoles [22, 23], and bowtie dipoles [24, 25], are popular choices for MI applications. Although these antennas have demonstrated effectiveness, there is always potential for further performance improvements.

This paper presents a monopole antenna with a cross slot for MI application. The overall antenna dimension is $50.4\times33.3\times1.6\,\mathrm{mm}^3$. The antenna boasts an operating bandwidth ranging from 1.76 to 13.6 GHz and a peak gain of 5.7 dBi at 8 GHz, all within a compact design. It delivers optimal performance in terms of reflection coefficient, voltage standing wave ratio (VSWR), gain, and efficiency, fulfilling the requirements for effective brain tumor detection and imaging.

The manuscript is organized as follows. Section 2 presents the modeling and analysis of the antenna, including parametric, time, and frequency domain analyses. Section 3 covers the design and simulation of the tumor model, along with its electric field (E-field) and magnetic field (H-field) analyses. Section 4 covers the fabrication of the tumor model and image reconstruction using the Delay and Sum (DAS) approach. Section 5 presents the final overview and conclusions of the research.

2. ANTENNA DEVELOPMENT AND EVALUATION

The preliminary design of the monopole antenna was based on the core principles and equations that govern microstrip antennas. These antennas are notable for their low profile, compact size, and lightweight nature, occupying minimal space. The fabrication process is straightforward, which simplifies the overall production, making it both easy and cost effective. Due to these economic advantages, microstrip antennas can be mass-produced using advanced modern printed circuit technologies. The initial antenna dimensions were calculated using Equations (1)–(3).

$$Wp = \frac{c}{2f_r}\sqrt{\frac{2}{\varepsilon_r+1}} \tag{1}$$

$$\varepsilon_{\mathit{reff}} = \frac{\varepsilon_r+1}{2}+\frac{\varepsilon_r-1}{2}\left[1+12\frac{h}{W}\right]^{-1/2} \tag{2}$$

$$L_P = \frac{c}{2f_r\sqrt{\varepsilon_{\mathit{reff}}}} \tag{3}$$

Here, f_r stands for the design frequency, c the speed of light, ϵ_r the permittivity of the substrate material, and h the height of the substrate. For antenna design, especially in biomedical applications, it is crucial to ensure that the dimensions of the antenna are compact.

2.1. Antenna Evolution

The proposed antenna evolution process involves a systematic and iterative approach in designing and optimizing a circular patch antenna with a central cross slot for biomedical applications. Starting with an initial design, a parametric study is employed to analyze the impact of various design parameters on the antenna performance. Through this evolution process, the development of a high-performance antenna that meets the need for microwave medical imaging is ensured.

The process of evolution centers on the development of a monopole antenna, given in Figs. 1(a)–(c). The initial version

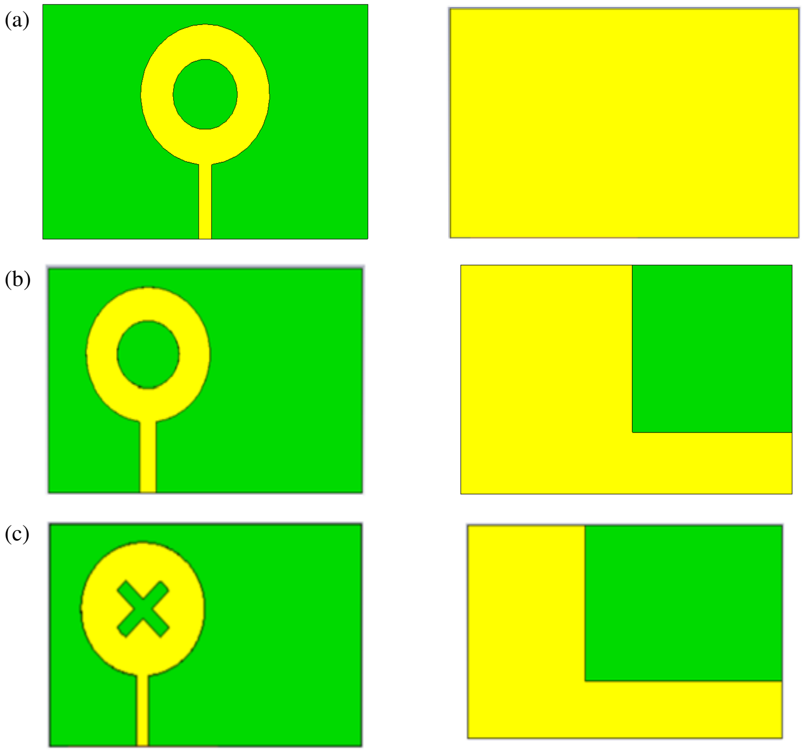

FIGURE 1. The various stages in the development of the antenna design. (a) Antenna 1, (b) Antenna-2 and (c) Antenna-3 (proposed).

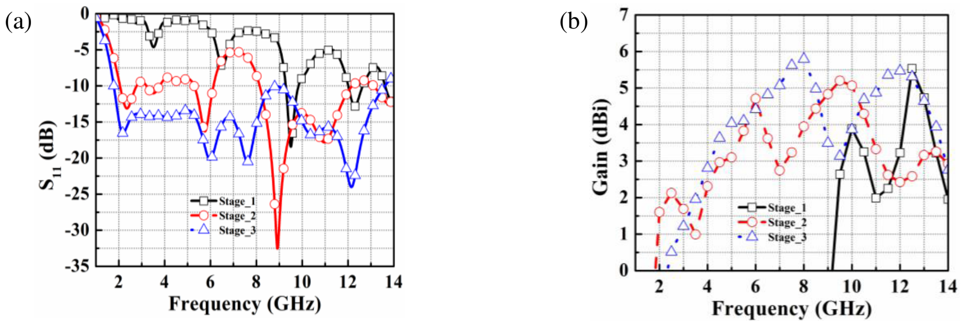

FIGURE 2. The performance parameters of the antenna design stages. (a) Return loss and (b) gain.

is denoted as Antenna-1, featuring a complete ground plane and a circular patch with a circular slot. This antenna is printed on a rectangular FR-4 substrate measuring 33.3×50.4 mm^2, with a relative permittivity of 4.4 and a thickness of 1.6 mm. In Fig. 1(b), a rectangular patch is etched out from the ground plane and is designated as Antenna-2. In this stage, the impedance matching performance is improved as compared to the previous stage. The final iteration, Antenna-3, which is the proposed version, incorporates a slotted cross-shaped patch configuration on the top, as well as extending the rectangular slot width in the ground plane, achieving the desired bandwidth along with enhanced gain performance. This version is depicted as Fig. 1(c). The return loss performance of the antenna at various design stages is observed and depicted in Fig. 2(a). It can be observed that in the case of Antenna-1, a return loss of less than -10 dB is observed from around 9.2 to 9.8 GHz. In the case of Antenna-2, the overall impedance matching performance is improved, and the antenna obtains a return loss of less than -10 dB from 8 to 12 GHz. It can be observed that the final stage (Antenna-3) obtains better performance than its initial design stages. This stage obtains a return loss of less than -10 dB from 1.76 to 13.6 GHz. Fig. 2(b) illustrates the gain performance respectively at different design stages in the development of the device. It can be observed that in Antenna-1, positive gain is obtained only in a small section of the operating band. In Antenna-2, the gain performance of the antenna is improved, and a peak gain around 5.2 dBi is obtained. In the final proposed stage (Antenna-3), a maximum gain of 5.7 dBi at 8 GHz is observed. The CST Microwave Studio 2018 Electromagnetic (EM) solver simulator is used to optimize the parameters of the proposed structure to accomplish the suitable bandwidth, gain, and radiation performance for imaging applications. The antenna architecture includes various parameters that have been adjusted to meet the required operating

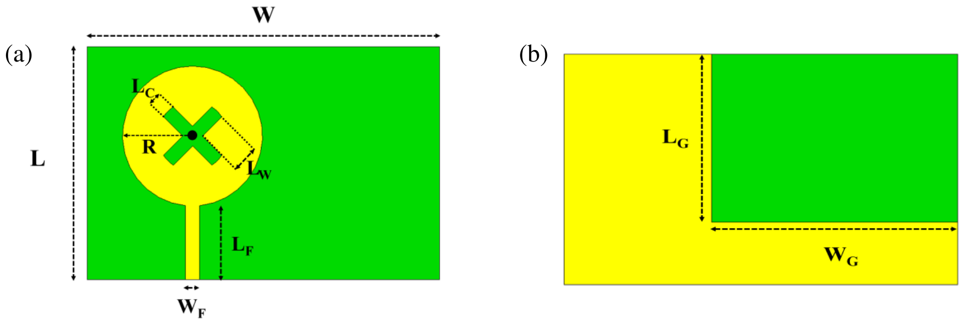

FIGURE 3. The configuration of the suggested antenna. (a) Frontal view and (b) rear view.

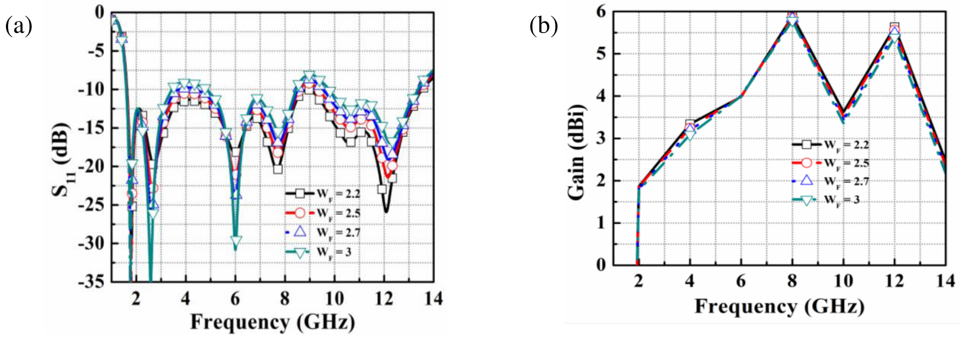

FIGURE 4. The performance metrices when the parameter W_F is varied. (a) Return loss and (b) gain.

TABLE 1. The specifications of the suggested antenna.

Parameter	Value	Parameter	Value	Parameter	Value	Parameter	Value	Parameter	Value
L	33.3	W	50.4	L_F	10.6	W_F	2.2	R	10
L_C	2	L_W	6	L_G	24.3	W_G	31.5	h	1.6

All dimensions are in "mm"

bandwidth and gain performance. Fig. 3 depicts the proposed antenna configuration with all the dimensions labeled. Here, Fig. 3(a) depicts the front view, and Fig. 3(b) depicts the back view of the proposed antenna. The overall dimensions and parameters of the proposed antenna are tabulated in Table 1 for better understanding and clarity. Here, L and W are the corresponding length and width of the proposed antenna. L_F is the feed length of the antenna, and W_F is the feed width. The circular patch is of radius R. L_C and L_D are the dimensions of the cross-slot present in the center of the circle-shaped patch. The rectangular slot in the ground plane is of dimensions $L_G \times W_G$.

2.2. Parametric Study

A parametric study is an exhaustive analysis that systematically investigates the influence of various design parameters on the performance of the antenna. This detailed investigation involves methodically varying specific parameters to understand their effects on key performance metrics like return loss and gain. The study is commenced by adjusting parameters such as feed width (W_F), radius of the circular patch (R), and cross-slot width (L_W). Initially, most of the parameter configurations did not yield a frequency band with a return loss below -10 dB, indicating poor performance. However, through a meticulous series of adjustments to the feed width, outer radius, and slot width, the operational bandwidth of the antenna was significantly improved. The optimized antenna exhibited a broad operational bandwidth ranging from 1.76 GHz to 13.6 GHz and a maximum gain performance around 5.8 dBi at 8 GHz.

Figure 4(a) depicts the return loss performance, and Fig. 4(b) depicts the gain performance metrices when the parameter W_F is varied. It can be observed that the return loss and gain performance vary for different dimensions. Finally, the value 2.2 mm was chosen for W_F as this produced the best result in terms of impedance matching and gain performance. Fig. 5(a) depicts the return loss performance, and Fig. 5(b) depicts the gain performance metrices when the parameter R is varied. The value 10 mm was chosen for R as this produced the best result in terms of impedance matching and gain performance. Fig. 6(a) depicts the return loss performance, and Fig. 6(b) depicts the gain performance metrices when the parameter L_W is varied. The value 6 mm was chosen for L_W as this produced the best result in terms of impedance matching and gain performance.

All the major simulated performance metrics of the proposed antenna are depicted in Fig. 7. Fig. 7(a) depicts the return

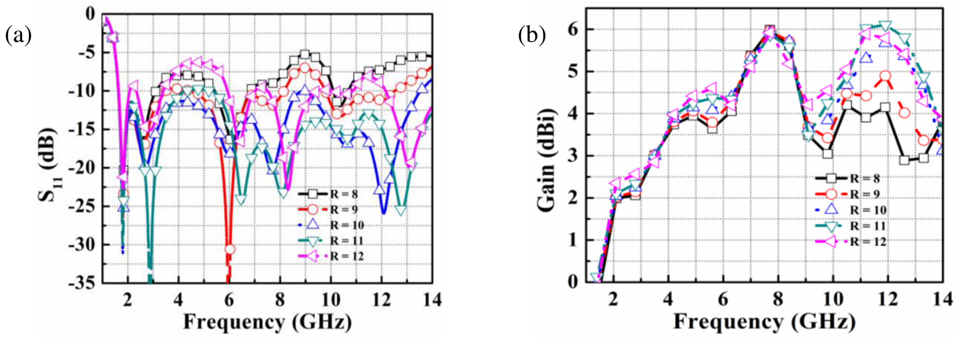

FIGURE 5. The performance metrices when the parameter R is varied. (a) Return loss and (b) gain.

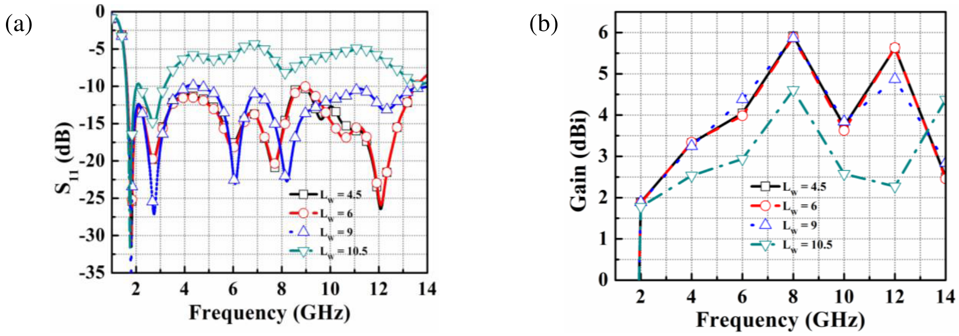

FIGURE 6. The performance metrices when the parameter L_W is varied. (a) Return loss and (b) gain.

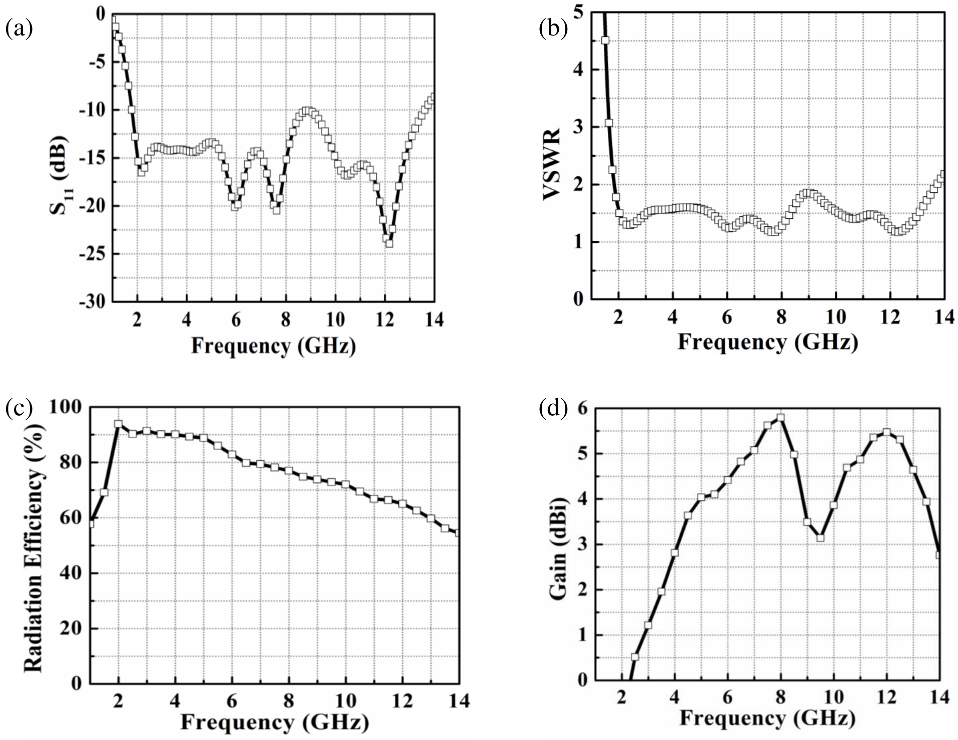

FIGURE 7. The simulated (a) return loss, (b) VSWR, (c) radiation efficiency, and (d) gain plot of the proposed antenna.

loss plot of the proposed antenna. It can be observed that the proposed antenna operates from 1.76 to 13.6 GHz with an impedance matching better than 10 dB. Fig. 7(b) depicts the VSWR plot of the proposed antenna. It can be observed that the proposed antenna attains a VSWR value less than 2 from 1.76 to 13.6 GHz. Fig. 7(c) depicts the radiation efficiency of the proposed antenna. It can be observed that the radiation efficiency is well above 80% in the obtained region of operation.

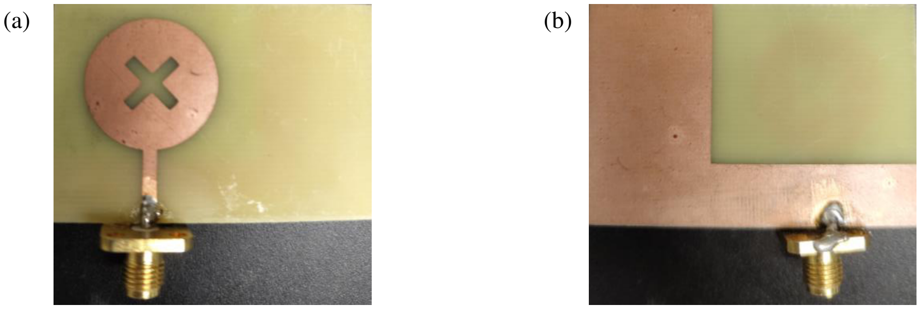

FIGURE 8. The fabricated antenna structure. (a) The front view and (b) the rear view.

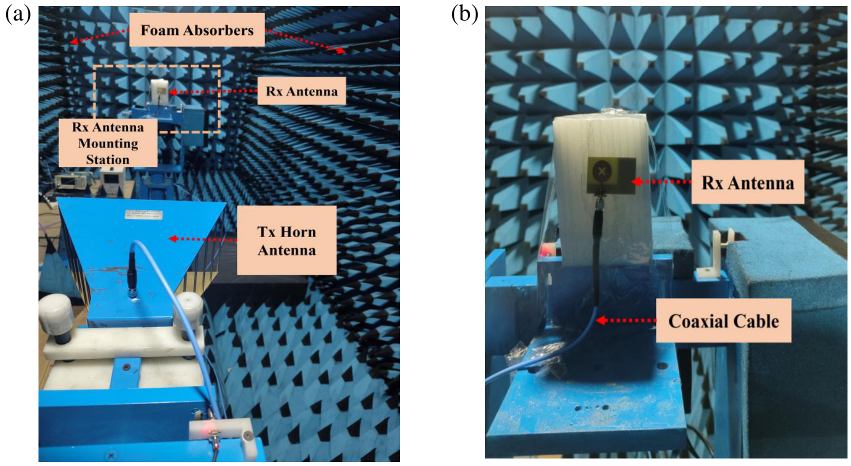

FIGURE 9. The antenna testing configuration. (a) The entire setup and (b) the zoomed-in view of the antenna.

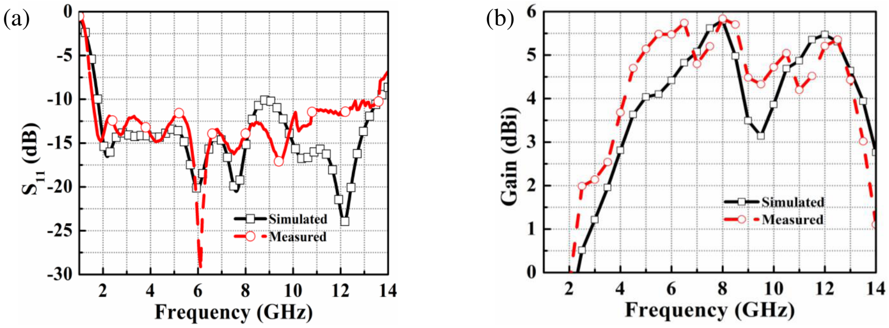

FIGURE 10. The measured v/s simulated response. (a) Return loss and (b) gain.

Finally, the gain plot of the proposed antenna is depicted in Fig. 7(d). It can be observed that the proposed antenna attains a peak gain of 5.8 dBi at 8 GHz.

2.3. Fabricated Antenna and Frequency Domain Analysis

Figure 8 displays the manufactured antenna, with Fig. 8(a) presenting the front view and Fig. 8(b) showing the rear view. The antenna is assembled on an FR-4 substrate, having a thickness of 1.6 mm, a dielectric constant of 4.4, and a loss tangent of 0.025. The testing of the antenna was carried out in an anechoic chamber, as outlined in Fig. 9. Fig. 9(a) presents the overall antenna measurement setup, illustrating the transmitting horn antenna as well as the surrounding foam absorbers, while Fig. 9(b) provides a magnified view of the antenna arrangement on the antenna mounting station, highlighting its configuration and setup in the testing environment.

Figure 10(a) displays the return loss plot for the suggested antenna, comparing the simulated and experimental results. The simulated and experimental responses show strong agreement, with the antenna showing a return loss of less than -10 dB across the frequency range from 1.76 GHz to 13.51 GHz. Fig. 10(b) shows the gain performance of the proposed antenna, comparing the results from simulation with those obtained from experiment. The data reveals a close match between the simulated and experimental gains, with the antenna achieving a peak gain of 5.8 dBi at 8 GHz. The

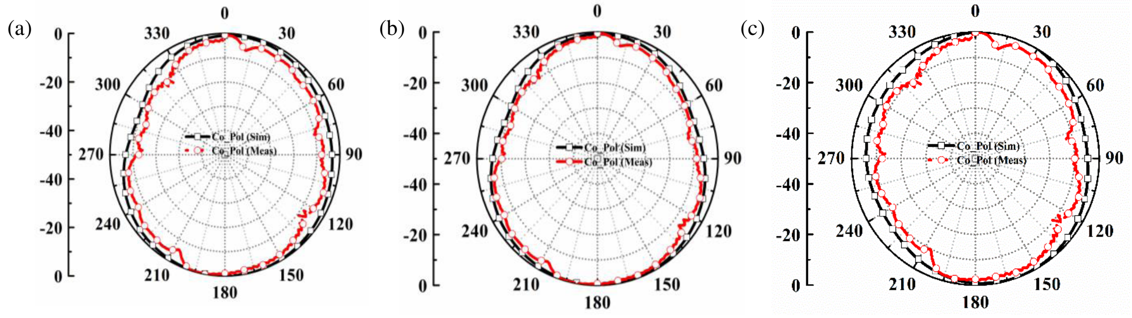

FIGURE 11. The simulated and measured E-plane radiation patterns of the antenna at (a) 3 GHz, (b) 4 GHz and (c) 6 GHz.

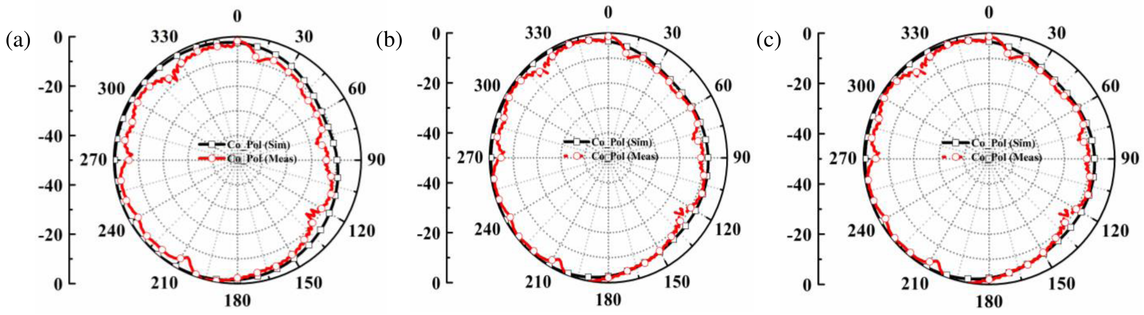

FIGURE 12. The simulated and measured H-plane radiation patterns of the antenna at (a) 3 GHz, (b) 4 GHz and (c) 6 GHz.

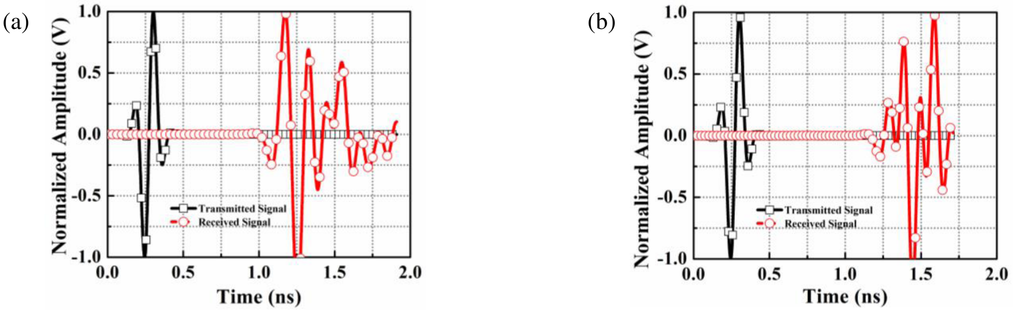

FIGURE 13. Normalized magnitude plots of the transmitted and received signals for: (a) FTF and (b) SBS configurations.

radiation pattern of the suggested antenna has been plotted and examined at different frequencies within its broadband range. Fig. 11 displays the E-plane radiation pattern of the suggested antenna, comparing the simulated and experimental results. The figure shows the radiation pattern at frequencies of (a) 3 GHz, (b) 4 GHz, and (c) 6 GHz. Simulated and experimental responses are consistent, as shown. Furthermore, Fig. 12 presents the radiation pattern in H-plane of the suggested antenna at these aforementioned frequencies. It can be observed that the simulated and actual results align closely. Minor differences between the simulated and experimental responses are attributed to losses from soldering, losses from the coaxial cable, connector losses, as well as losses due to antenna alignment in the antenna mounting station.

2.4. Time Domain Analysis

A comprehensive analysis of the time-domain characteristics of the antenna was conducted to assess its suitability for MI. This included assessing transmitted and received signals, as well as metrics such as Fidelity Factor (FF) and Group Delay (GD). The evaluations were conducted with two setups: Face-To-Face (FTF) and Side-By-Side (SBS), with a 200 mm separation between the antennas in each configuration. Fig. 13(a) depicts the normalized magnitude for the FTF arrangement, and Fig. 13(b) shows it for the SBS arrangement. The FTF configuration demonstrates better signal alignment and stronger guided radiation than the lateral setup, making it more effective for brain tumor imaging applications.

Equation (4) is used to assess the cross-correlation between the transmitted and received signals, a measure known as FF [26]. This factor quantifies the degree of similarity and accuracy between the two signals.

$$\mathrm{FF} = \max_{\tau}\left|\frac{\int_{-\infty}^{+\infty} S\left(t\right) r(t-\tau)dt}{\int_{-\infty}^{+\infty} S(t)^{2}.\int_{-\infty}^{+\infty} r(t)^{2}dt}\right| \tag{4}$$

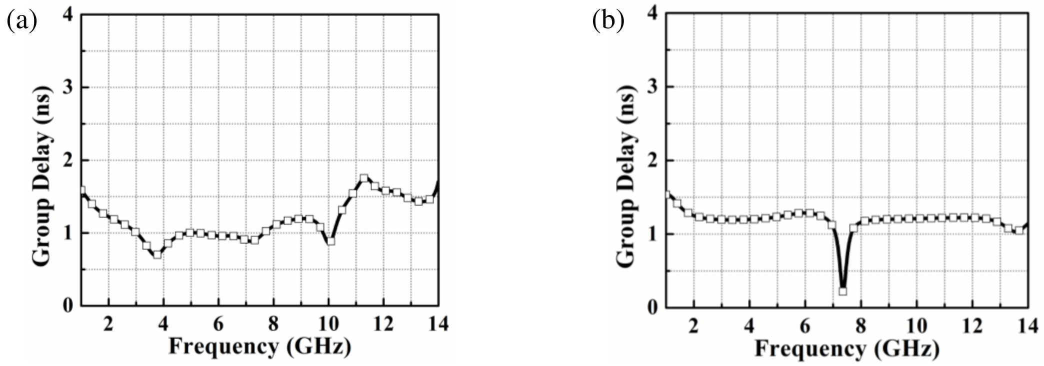

FIGURE 14. The simulated GD for (a) FTF configuration and (b) SBS configuration.

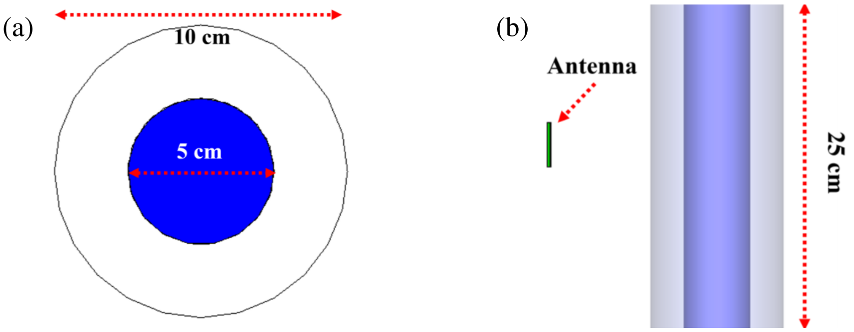

FIGURE 15. The modelled brain tumor model in the simulator. (a) Top view and (b) side view.

In this analysis, $s(t)$ and $r(t)$ correspond to the transmitted and received signals, respectively, and τ represents the GD. The FF measurements show 70.41% for the FTF configuration and 51.31% for the SBS configuration. The high FF value for the FTF arrangement indicates that the transmitted signal is minimally distorted in this setup. This indicates that the arrangement effectively preserves the integrity of the transmitted signal, resulting in a clearer and more accurate reception.

Another important aspect in assessing the time-domain performance of the antenna is the GD, which reflects the phase distortion of the signal. It is defined as the negative rate of change of the phase of the transfer function, $\varphi(\omega)$, with respect to frequency [26]. Group delay estimates the duration a signal requires to traverse the antenna. It is determined using Equation (5), as shown below:

$$\tau(\omega) = -\frac{d\varphi(\omega)}{d\omega} = -\frac{d\varphi(\omega)}{2\pi df} \tag{5}$$

For wideband applications, a consistent group delay response is vital to preserve signal quality. Fig. 14 shows the simulated group delay for the proposed antenna across two different setups. The FTF setup maintains group delay variations within 1.74 ns, indicating stable performance, while the lateral configuration exhibits significant distortion, affecting signal quality. Thus, for brain tumor detection, the FTF configuration is preferred due to its improved accuracy and consistency.

3. BRAIN TUMOR MODELLING AND PERFORMANCE ASSESSMENT

3.1. Brain Tumor Modelling in the Simulator

To detect brain tumor in the simulator, an appropriate model has been made in the simulator. The designed model consists of a cylindrical foam of diameter 100 mm and height 250 mm. A supplementary cylinder, measuring 50 mm in diameter and 250 mm in height, is placed within the foam. This new cylinder, made of water, is used to simulate the properties of blood in the brain. Fig. 15 presents the setup from various angles: Fig. 15(a) depicts the top view, and Fig. 15(b) shows the side view of the complete arrangement with labeling. The depicted setup has been arranged practically as given in the figure to enable the detection of brain tumors.

3.2. E-Field and H-Field Analysis

An in-depth study of how the E-field and H-field penetrate materials was conducted to thoroughly evaluate the antenna performance for MI. Figs. 16(a)–(c) display the penetration of the E-field through the XZ-plane of the modelled tumor model at 3 GHz, 6 GHz, and 9 GHz. These visuals demonstrate that the E-field penetrates the model thoroughly, reaching substantial depths at each frequency. Figs. 17(a)–(c) show H-field penetration at the same frequencies. While H-field intensity decreases due to the lossy nature of the model, the propagation of the antenna enhances the field infiltration. This comprehensive

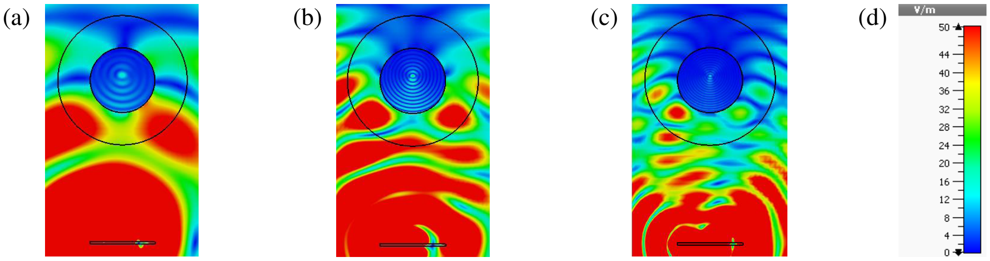

FIGURE 16. The distribution of the E-field produced by the antenna with the brain tumor model at (a) 3 GHz, (b) 6 GHz, and (c) 9 GHz. The scaling provided in (d).

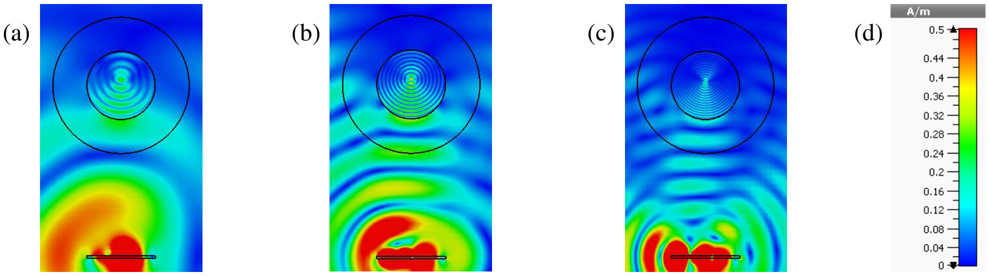

FIGURE 17. The distribution of the H-field produced by the antenna with the brain tumor model at (a) 3 GHz, (b) 6 GHz, and (c) 9 GHz. The scaling provided in (d).

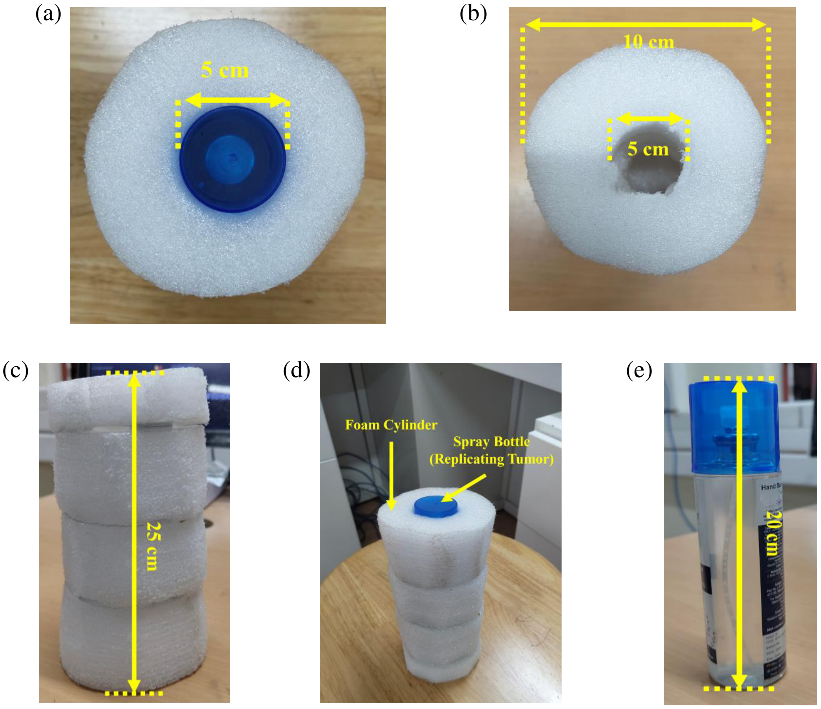

FIGURE 18. The fabricated tumor model. (a) The model top view with target, (b) the model top view without the target, (c) the complete model perspective view, (d) the perspective view with the target and (e) cylindrical target.

analysis confirms the capability of the device to penetrate the model effectively, which is essential for capturing critical information for accurate target imaging. The strong electromagnetic field penetration across various frequencies is crucial for high-quality MI applications, ensuring effective imaging and diagnostic capability.

4. TUMOR MODELLING IN A PRACTICAL SETTING AND IMAGING

4.1. Tumor Modelling

The tumor is modelled as depicted in Fig. 18. Fig. 18(a) shows the top view of the foam structure with the target inserted. The

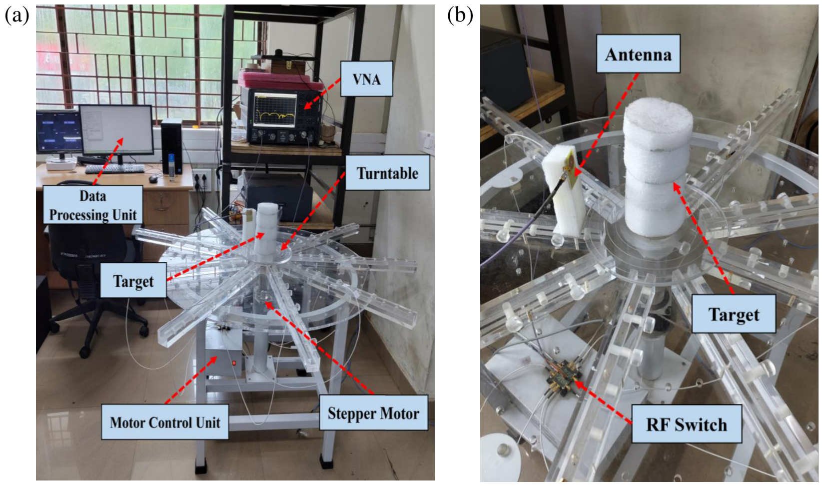

FIGURE 19. The imaging system implemented in the proposed approach. (a) Entire setup, and (b) magnified view of the antenna and the target.

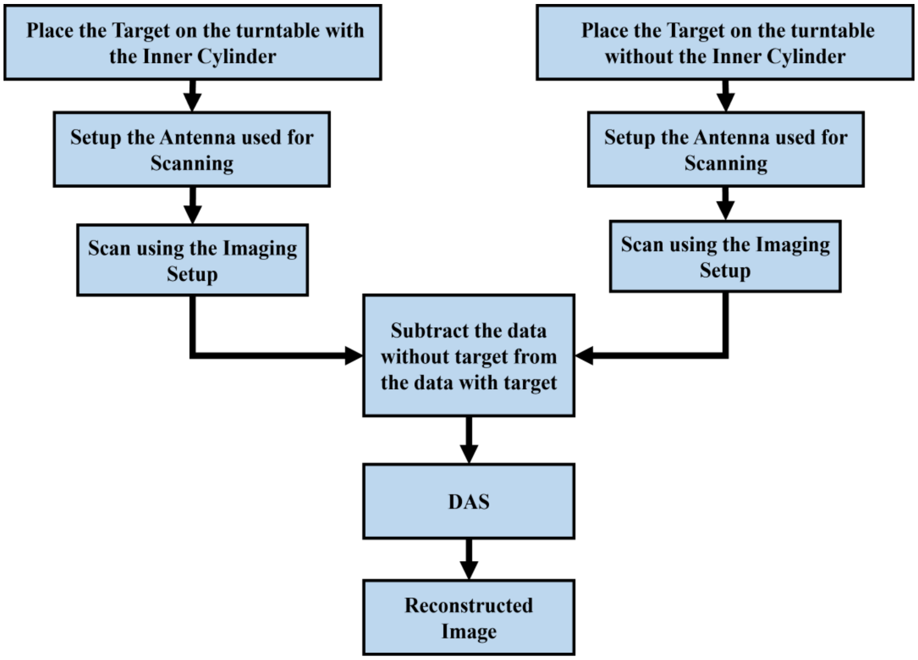

FIGURE 20. The imaging process flow chart.

target is a cylinder of diameter 5 cm and height 20 cm, as depicted in the figure. Fig. 18(b) depicts the same structure without the target. Fig. 18(c) shows the perspective view of the same structure. The total length of the foam structure can be understood from this figure. The perspective view of the foam cylinder with the target inserted is depicted in Fig. 18(d). The target is separately shown in Fig. 18(e).

4.2. Imaging of the Tumor Model

Figure 19 depicts the imaging setup used in this study, employing a monostatic approach for image reconstruction. The target is positioned on a turntable and is rotated in 40-degree increments. This configuration yields nine S_{11} readings per rotation from the Vector Network Analyzer (VNA), which are subsequently captured by the interfaced computer. The antenna functions as both the transmitter and receiver. Data from the frequency domain, acquired during each rotation from the VNA, is converted to time domain and then used in conjunction with the DAS method to reconstruct the image.

In the DAS process, time-shifted backscattered signals from the target are combined to form a synthetic focus. This approach amplifies the signal strength at resonant frequencies, enhancing the imaging accuracy.

The signal magnitudes at each focus point are recorded and visualized in MATLAB, with the general DAS expression given in Equation (6).

$$Y_{\text{DAS}} = \sum_{I=1}^{M} \left| b_i \left(t - \tau \right) \right| \tag{6}$$

TABLE 2. A comprehensive comparison of the proposed antenna with similar works.

Ref.	Antenna structure	Dimensions (mm^3)	Name of substrate	Operating band (GHz), FBW (%)	Re. Gain (dBi)	FF %	No of Antennas & Simulated/Measured	Tested Phantom Model
[27]	W-shaped slot-loaded U-shaped low SAR patch antenna	56× 37× 1.6	FR4	1.40–2.52, 57.14%	3.5	80	Nine antennas, Simulated	Simulated Hugo head model
[28]	Cross-split ring resonator metamaterial antenna	31.7× 24× 1.6	FR4	0.75–1.60, 72.3	NG	NG	Twelve antennas, Simulated	3D SAM head phantom model
[29]	Grounded coplanar waveguide slotted inverted delta antenna	50× 44× 1.524	Rogers RO4350B	1.70–3.71, 74.30	5.65	98	Twelve antennas, Simulated	Simulated Hugo head model
[30]	Three-dimensional (3D) directive microwave antenna	40× 25× 10.5	Copper sheet	1.67–1.74, 4.10%	5.2	NG	Two antennas, Simulated	Simulated head model
[31]	Three-dimensional (3D) slot rotated wideband antenna	50× 25× 1.6	FR4	1.41–3.57, 87%	2.6	NG	Single antenna, Experimental	3D SAM head phantom model
[32]	Compact Unidirectional Conformal Antenna	25× 28× 5.6	PDMS-Al_2O_3-G	1.00–4.30, 124%	NG	92	Thirteen antennas, Experimental	Liquid head phantom model
[33]	Brick shaped printed monopole antenna	70× 50× 1.55	FR4	0.80–1.20, 40%	NG	NG	Two antennas, Simulated	3D plastic head model
[34]	Double hollow rectangular patch with slotted ground antenna	70× 60× 1.6	FR4	1.22–3.04, 85.71%	5	92.7	Nine antennas, Simulated	Simulated Hugo head model
[35]	Compact ultra-wideband (UWB) bowtie antenna	60× 60× 50	Rogers RO4003C	1–6, 143%	NG	81	Eight antennas, Simulated & Experimental	Liquid head phantom model
[36]	Miniaturized high-fidelity ultra-wideband (UWB) Slot Antenna	20× 20× 0.8	FR4	3.19–10.73, > 100%	NG	> 80	Eighteen antennas, Simulated	Simulated head model
[37]	Ultra-wideband (UWB) rectangular patch antenna	38× 25× 1.73	FR4	5.16–8.4, 47.09%	3.33	NG	Single antenna, Simulated	Simulated head model
[38]	Coplanar waveguide-fed split-ring resonator antenna	24× 24× 1.6	FR4	0.5–6, 169%	NG	> 70	Single antenna, Simulated	Simulated head model
[39]	Zero-Index Metamaterial Superstrates ultra-wideband (UWB) Antenna	110× 65× 0.51	Rogers RT5880	0.5–3.5, 150%	5.7	NG	Single antenna, Experimental	Liquid head phantom model
[40]	Circular slotted patch with defected grounded monopole patch antenna	70× 60× 1.5	FR4	1.22–3.45, 95.71%	5	92	Nine antennas, Simulated	Simulated Hugo head model
[41]	Ultra-wideband (UWB) patch antenna using graphene-based conductor (GBC)	22× 12× 1.52	Rogers laminate TMM4	3.15–9.15, 97.5%	NG	NG	Single antenna, Simulated	Simulated head model
This Work	**UWB Monopole antenna with cross-slot**	**50.4× 33.3× 1.6**	**FR4**	**1.7–13.6, 155.55 %**	**5.8**	**70.41**	**Single antenna, Simulated**	**Liquid Bottle covered by Foam material**

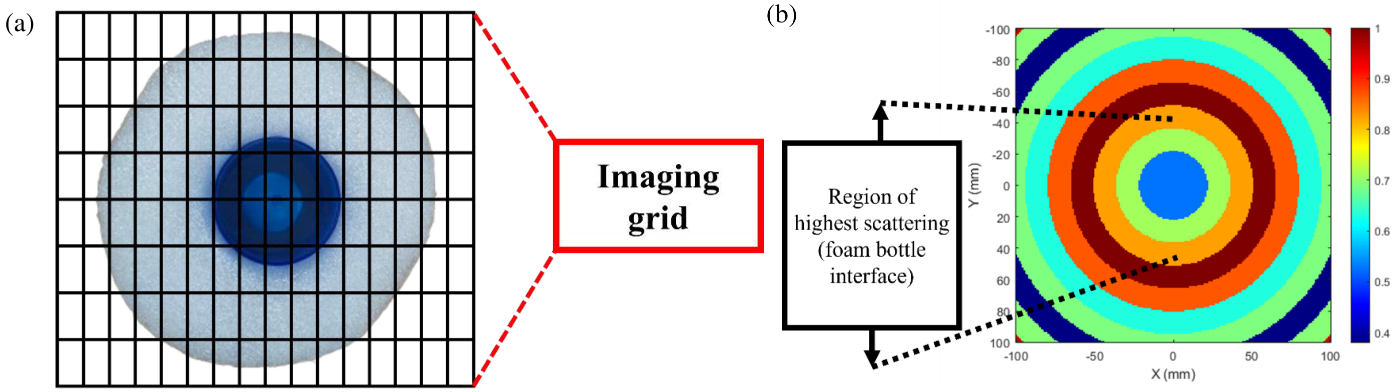

FIGURE 21. The (a) top view of target with the imaging grid and (b) the reconstructed images of the target using the DAS approach. The region of the highest scattering is displayed in the inset.

Y_{DAS} indicates the final output of the DAS technique, and $b_i(t-\tau)$ refers to the delay compensation. The image reconstruction procedure is summarized in the flowchart in Fig. 20. The top view of target with the imaging grid is depicted in Fig. 21(a), and the reconstructed image of the target using the DAS approach is depicted in Fig. 21(b). It can be observed that the target has been reconstructed up to a reasonable extent. Small deviations from the true target positions are observed, which may result from measurement inaccuracies, nearby interference, and cable losses. A comparison of the suggested antenna with other antennas is presented in Table 2, highlighting its superior performance for microwave head imaging.

5. CONCLUSION

The proposed work introduces an antenna operating within the 1.76–13.6 GHz range, featuring a peak gain of 5.8 dBi at 8 GHz, specifically designed for brain tumor detection. Comprehensive evaluations of the antenna in both frequency and time domains are extensively detailed. The antenna has been tested in an anechoic chamber environment, and the results are found to have a good handshake with its simulated counterpart. A high dielectric target was chosen for testing in the lab. The antenna was employed to image this target using the fundamental DAS approach. The target has been reconstructed successfully. Future work will involve using the antenna with various algorithms to image complex targets and incorporating several clutter removal techniques to minimize false positive signals. Moreover, the fabricated antenna with multiple copies of the same will be employed for inspecting various hidden metallic and non-metallic items using a multistatic approach.

ACKNOWLEDGEMENT

The authors would like to express their profound gratitude to the IIT Mandi iHUB and HCI foundation under project number IIT MANDI iHub/RD/2023-2025/03 and Science and Engineering Research Board, Government of India under project number TTR/2022/000001, for partially funding of this work. The authors would also like to thank the director of Indian Institute of Technology Palakkad for setting up the Central Instrumentation Facility.

REFERENCES

[1] Siegel, R. L., A. N. Giaquinto, and A. Jemal, "Cancer statistics, 2024," *CA: A Cancer Journal for Clinicians*, Vol. 74, No. 1, 12–49, 2024.

[2] Miller, B. A., K. C. Chu, B. F. Hankey, and L. A. G. Ries, "Cancer incidence and mortality patterns among specific Asian and Pacific Islander populations in the U.S." *Cancer Causes & Control*, Vol. 19, 227–256, 2008.

[3] Ostrom, Q. T., M. Price, K. Ryan, J. Edelson, C. Neff, G. Cioffi, K. A. Waite, C. Kruchko, and J. S. Barnholtz-Sloan, "CBTRUS statistical report: Pediatric brain tumor foundation childhood and adolescent primary brain and other central nervous system tumors diagnosed in the United States in 2014-2018," *Neuro-Oncology*, Vol. 24, No. 3, iii1–iii38, 2022.

[4] Ostrom, Q. T., M. Price, C. Neff, G. Cioffi, K. A. Waite, C. Kruchko, and J. S. Barnholtz-Sloan, "CBTRUS statistical report: Primary brain and other central nervous system tumors diagnosed in the United States in 2016-2020," *Neuro-Oncology*, Vol. 25, No. 4, iv1–iv99, Oct. 2023.

[5] Bhimani, A. D., S. Denyer, D. R. Esfahani, J. Zakrzewski, T. M. Aguilar, and A. I. Mehta, "Surgical complications in intradural extramedullary spinal cord tumors-an ACS-NSQIP analysis of spinal cord level and malignancy," *World Neurosurgery*, Vol. 117, e290–e299, 2018.

[6] Asok, A. O., G. N. S. J., and S. Dey, "Non-invasive breast tumor detection with antipodal vivaldi antenna using monostatic approach," *International Journal of RF and Microwave Computer-Aided Engineering*, Vol. 32, No. 12, e23539, 2022.

[7] Fiser, O., M. Helbig, J. Sachs, S. Ley, I. Merunka, and J. Vrba, "Microwave non-invasive temperature monitoring using UWB radar for cancer treatment by hyperthermia," *Progress In Electromagnetics Research*, Vol. 162, 1–14, 2018.

[8] Grzegorczyk, T. M., P. M. Meaney, P. A. Kaufman, R. M. di-Florio Alexander, and K. D. Paulsen, "Fast 3-D tomographic microwave imaging for breast cancer detection," *IEEE Transactions on Medical Imaging*, Vol. 31, No. 8, 1584–1592, Aug. 2012.

[9] Tobon Vasquez, J. A., R. Scapaticci, G. Turvani, G. Bellizzi, D. O. Rodriguez-Duarte, N. Joachimowicz, B. Duchêne,

E. Tedeschi, M. R. Casu, L. Crocco, and F. Vipiana, "A prototype microwave system for 3D brain stroke imaging," *Sensors*, Vol. 20, No. 9, 2607, 2020.

[10] Merunka, I., A. Massa, D. Vrba, O. Fiser, M. Salucci, and J. Vrba, "Microwave tomography system for methodical testing of human brain stroke detection approaches," *International Journal of Antennas and Propagation*, Vol. 2019, No. 1, 4074862, Mar. 2019.

[11] Rahama, Y. A., O. A. Aryani, U. A. Din, M. A. Awar, A. Zakaria, and N. Qaddoumi, "Novel microwave tomography system using a phased-array antenna," *IEEE Transactions on Microwave Theory and Techniques*, Vol. 66, No. 11, 5119–5128, Nov. 2018.

[12] Dachena, C., A. Fedeli, A. Fanti, M. B. Lodi, M. Pastorino, and A. Randazzo, "Microwave imaging for the diagnosis of cervical diseases: A feasibility analysis," *IEEE Journal of Electromagnetics, RF and Microwaves in Medicine and Biology*, Vol. 5, No. 3, 277–285, Sep. 2021.

[13] Amin, B., A. Shahzad, L. Crocco, M. Wang, M. O'Halloran, A. González-Suárez, and M. A. Elahi, "A feasibility study on microwave imaging of bone for osteoporosis monitoring," *Medical & Biological Engineering & Computing*, Vol. 59, 925–936, 2021.

[14] Sachs, J., S. Ley, T. Just, S. Chamaani, and M. Helbig, "Differential ultra-wideband microwave imaging: Principle application challenges," *Sensors*, Vol. 18, No. 7, 2136, Jul. 2018.

[15] Fear, E. C., X. Li, S. C. Hagness, and M. A. Stuchly, "Confocal microwave imaging for breast cancer detection: Localization of tumors in three dimensions," *IEEE Transactions on Biomedical Engineering*, Vol. 49, No. 8, 812–822, Aug. 2002.

[16] Song, H., S. Sasada, T. Kadoya, M. Okada, K. Arihiro, X. Xiao, and T. Kikkawa, "Detectability of breast tumor by a hand-held impulse-radar detector: Performance evaluation and pilot clinical study," *Scientific Reports*, Vol. 7, No. 1, 16353, 2017.

[17] Baran, A., D. J. Kurrant, A. Zakaria, E. C. Fear, and J. LoVetri, "Breast imaging using microwave tomography with radar-based tissue-regions estimation," *Progress In Electromagnetics Research*, Vol. 149, 161–171, 2014.

[18] Sabouni, A., D. Flores-Tapia, S. Noghanian, G. Thomas, and S. Pistorius, "Hybrid microwave tomography technique for breast cancer imaging," in *2006 International Conference of the IEEE Engineering in Medicine and Biology Society*, 4273–4276, Aug. 2006.

[19] Bourqui, J., M. Okoniewski, and E. C. Fear, "Balanced antipodal vivaldi antenna with dielectric director for near-field microwave imaging," *IEEE Transactions on Antennas and Propagation*, Vol. 58, No. 7, 2318–2326, Jul. 2010.

[20] Li, X., S. C. Hagness, M. K. Choi, and D. W. V. D. Weide, "Numerical and experimental investigation of an ultrawideband ridged pyramidal horn antenna with curved launching plane for pulse radiation," *IEEE Antennas and Wireless Propagation Letters*, Vol. 2, 259–262, 2003.

[21] Di Clemente, F. S., M. Helbig, J. Sachs, U. Schwarz, R. Stephan, and M. A. Hein, "Permittivity-matched compact ceramic ultra-wideband horn antennas for biomedical diagnostics," in *Proceedings of the 5th European Conference on Antennas and Propagation (EUCAP)*, 2386–2390, Rome, Italy, Apr. 2011.

[22] Jafari, H. M., M. J. Deen, S. Hranilovic, and N. K. Nikolova, "A study of ultrawideband antennas for near-field imaging," *IEEE Transactions on Antennas and Propagation*, Vol. 55, No. 4, 1184–1188, Apr. 2007.

[23] Alam, A. H. M. Z., M. R. Islam, and S. Khan, "Design and analysis of UWB rectangular patch antenna," in *2007 Asia-Pacific Conference on Applied Electromagnetics*, 1–3, Melaka, Malaysia, Dec. 2007.

[24] Yurduseven, O., D. Smith, and M. Elsdon, "Printed slot loaded bow-tie antenna with super wideband radiation characteristics for imaging applications," *IEEE Transactions on Antennas and Propagation*, Vol. 61, No. 12, 6206–6210, Dec. 2013.

[25] Kanj, H. and M. Popovic, "Miniaturized microstrip-fed "dark eyes" antenna for near-field microwave sensing," *IEEE Antennas and Wireless Propagation Letters*, Vol. 4, 397–401, 2005.

[26] Asok, A. O., A. Tripathi, and S. Dey, "Breast tumors detection using multistatic microwave imaging with antipodal Vivaldi antennas utilizing DMAS and it-DMAS techniques," *International Journal of Microwave and Wireless Technologies*, Vol. 16, No. 4, 1–14, 2024.

[27] Alam, M. M., M. S. Talukder, M. Samsuzzaman, A. I. Khan, N. Kasim, I. M. Mehedi, and R. Azim, "W-shaped slot-loaded U-shaped low SAR patch antenna for microwave-based malignant tissue detection system," *Chinese Journal of Physics*, Vol. 77, 233–249, 2022.

[28] Razzicchia, E., I. Sotiriou, H. Cano-Garcia, E. Kallos, G. Palikaras, and P. Kosmas, "Feasibility study of enhancing microwave brain imaging using metamaterials," *Sensors*, Vol. 19, No. 24, 5472, 2019.

[29] Hossain, A., M. T. Islam, M. E. H. Chowdhury, and M. Samsuzzaman, "A grounded coplanar waveguide-based slotted inverted delta-shaped wideband antenna for microwave head imaging," *IEEE Access*, Vol. 8, 185 698–185 724, 2020.

[30] Ullah, M. A., T. Alam, and M. T. Islam, "A 3D directive microwave antenna for biomedical imaging application," *Bulletin of the Polish Academy of Sciences. Technical Sciences*, Vol. 66, No. 3, 355–360, 2018.

[31] Rezaeieh, S. A., A. Zamani, and A. M. Abbosh, "3-D wideband antenna for head-imaging system with performance verification in brain tumor detection," *IEEE Antennas and Wireless Propagation Letters*, Vol. 14, 910–914, 2014.

[32] Alqadami, A. S. M., N. Nguyen-Trong, B. Mohammed, A. E. Stancombe, M. T. Heitzmann, and A. Abbosh, "Compact unidirectional conformal antenna based on flexible high-permittivity custom-made substrate for wearable wideband electromagnetic head imaging system," *IEEE Transactions on Antennas and Propagation*, Vol. 68, No. 1, 183–194, 2019.

[33] Rodriguez-Duarte, D. O., J. A. T. Vasquez, R. Scapaticci, L. Crocco, and F. Vipiana, "Brick-shaped antenna module for microwave brain imaging systems," *IEEE Antennas and Wireless Propagation Letters*, Vol. 19, No. 12, 2057–2061, Dec. 2020.

[34] Samsuzzaman, M., K. A. Fakeeh, M. S. Talukder, M. M. Hasan, M. H. Rahman, M. M. Alam, M. S. Shaik, and M. T. Islam, "A double hollow rectangular-shaped patch and with the slotted ground plane monopole wideband antenna for microwave head imaging applications," *International Journal of Communication Systems*, Vol. 34, No. 16, e4958, 2021.

[35] Fiser, O., V. Hruby, J. Vrba, T. Drizdal, J. Tesarik, J. V. Jr, and D. Vrba, "UWB bowtie antenna for medical microwave imaging applications," *IEEE Transactions on Antennas and Propagation*, Vol. 70, No. 7, 5357–5372, Jul. 2022.

[36] Ojaroudi, M., S. Bila, and M. Salimi, "A novel approach of brain tumor detection using miniaturized high-fidelity UWB slot antenna array," in *2019 13th European Conference on Antennas and Propagation (EuCAP)*, 1–5, Krakow, Poland, 2019.

[37] Goswami, N. and M. A. Rahman, "Design of a UWB patch antenna and performance evaluation in detecting brain tumors," *E-Prime — Advances in Electrical Engineering, Electronics and Energy*, Vol. 8, 100623, 2024.

[38] Goodarzi, P., "A novel UWB antenna integrated with active circuit for high resolution near field microwave brain imaging," *Authorea Preprints*, 2023.

[39] Jamlos, M. A., N. A. Othman, W. A. Mustafa, M. F. Jamlos, and M. N. K. H. Rohani, "Zero-index metamaterial superstrates UWB antenna for microwave imaging detection," *Computers, Materials & Continua*, Vol. 75, 277–292, 2023.

[40] Samsuzzaman, M., M. S. Talukder, A. Alqahtani, A. G. Alharbi, R. Azim, M. S. Soliman, and M. T. Islam, "Circular slotted patch with defected grounded monopole patch antenna for microwave-based head imaging applications," *Alexandria Engineering Journal*, Vol. 65, 41–57, 2023.

[41] Aziz, M. A. I., M. M. Rana, M. A. Islam, and R. Inum, "Effective modeling of GBC based ultra-wideband patch antenna for brain tumor detection," in *2018 International Conference on Computer, Communication, Chemical, Material and Electronic Engineering (IC4ME2)*, 1–4, Rajshahi, Bangladesh, Feb. 2018.